

Fully Automatic In-Situ Reconfiguration of RF Photonic Filters in a CMOS-Compatible Silicon Photonic Process

MD JUBAYER SHAWON,^{1,*} AND VISHAL SAXENA¹

¹*Department of Electrical and Computer Engineering, University of Delaware, Newark, Delaware 19716, USA*

**shawon@udel.edu*

Abstract: Automatic reconfiguration of optical filters is the key to novel flexible RF photonic receivers and Software Defined Radios (SDRs). Although silicon photonics (SiP) is a promising technology platform to realize such receivers, process variations and lack of in-situ tuning capability limits the adoption of SiP filters in widely-tunable RF photonic receivers. To address this issue, this work presents a first ‘in-situ’ automatic reconfiguration algorithm and demonstrates a software configurable integrated optical filter that can be reconfigured on-the-fly based on user specifications. The presented reconfiguration scheme avoids the use of expensive and bulky equipment such as Optical Vector Network Analyzer (OVNA), does not use simulation data for reconfiguration, reduces the total number of thermo-optic tuning elements required and eliminates several time consuming configuration steps as in the prior art. This makes this filter ideal in a real world scenario where user specifies the filter center frequency, bandwidth, required rejection & filter type (Butterworth, Chebyshev, etc.) and the filter is automatically configured regardless of process, voltage & temperature (PVT) variations. We fabricated our design in AIM Photonics’ Active SiP process and have demonstrated our reconfiguration algorithm for a second-order filter with 3dB bandwidth of 3 GHz, 2.2 dB insertion loss and >30 dB out-of-band rejection using only two reference laser wavelength settings. Since the filter photonic integrated circuit (PIC) is fabricated using a CMOS-compatible SiP foundry, the design is manufacturable with repeatable and scalable performance suited for its integration with electronics to realize complex chip-scale RF photonic systems.

© 2022 Optica Publishing Group under the terms of the [Optica Publishing Group Publishing Agreement](#)

1. Introduction

Integrated radio-frequency (RF) photonics is rapidly emerging as a technology enabler of demanding application scenarios which require capabilities beyond those of traditional electronic systems. These capabilities include ultra-wide bandwidth, exceptional low latency, long-distance routing and immunity to electromagnetic interference (EMI) [1–6]. For any RF photonic integrated circuit (IC), optical filters are essential building blocks. The desirable feature that distinguishes RF photonic filters from their electronic, microwave and micro-electromechanical systems (MEMS) counterparts is their tunability over a very wide range of center frequencies (1 to 100s of GHz) and very wide bandwidth. Consequently, RF photonic filters offer unprecedented reconfiguration capabilities (center frequency, bandwidth, filter type, and rejection) that is inconceivable with electronic ICs alone [2, 6]. However, for their wider adoption in frequency-agile RF photonic receivers or Software Defined Radios (SDR), filter reconfiguration has to be rapid and in-situ, *i.e.*, automatic and free from any manual intervention [7].

Traditionally, RF photonic systems have been implemented using discrete and bulky photonic components that are power inefficient, expensive and most importantly, are not amenable to integration of complex systems. Silicon Photonics, on the other hand, leverages the unique capabilities of photonic signal processing while takes full advantage of the mature CMOS

fabrication processes developed by the semiconductor industry [7–9]. This means, an optical filter realized in a silicon photonic platform is area and power efficient, robust, scalable and can be manufactured on large-scale at lower cost. However, due to process-induced random variations, any filter designed in a silicon photonic process will deviate from its intended characteristics. Therefore, a scheme is required that not only reconfigures the filter automatically but also is robust against process, voltage and temperature (PVT) variations.

Reconfiguration and tuning of integrated optical filters has been pursued in the literature. In ref. [10], only center frequency tuning was addressed whereas in refs. [11–14], both center frequency and bandwidth were tunable. However, none of these works pursued out-of-band rejection tuning in the filter. Moreover, the filter reconfiguration was not fully automatic and heavily relied upon manual tuning. The first fully automatic tuning of silicon photonic filter was demonstrated by Choo et. al. in ref. [7]. However, the reconfiguration process involved the use of bulky and cost prohibitive equipment such as an Optical Vector Network Analyzer (OVNA) to extract ring losses using Jones Matrix based method [7, 15].

The fundamental novelty of this work is that it achieves a truly in-situ automatic optical filter reconfiguration solution that has been experimentally demonstrated using a CMOS-compatible silicon-on-insulator (SOI) photonic process. We present an algorithm different from the one in ref. [7] which precludes the use of OVNA and eliminates several time consuming steps during the reconfiguration process. In addition, our filter also uses less number of thermal tuning elements than [7]. The designed filter has a compact form factor and is the first such filter fabricated in AIM Photonics' active photonic process by leveraging proven process development kit (PDK) library components.

2. Filter design, fabrication and Packaging

2.1. Filter Topology

The schematics of the coupled all-pass decomposition (APD) filter structure [16, 17] is shown in **Fig. 1**. Here, grating couplers and 4-channel fiber array with polarization maintaining fibers are used to couple the light in and out of the chip. The input laser is fed to both arms of an outer Mach Zehnder Interferometer (MZI) through a 3dB coupler. Each arm of the MZI is loaded with a microring (UR/LR) via a tunable coupler (UR-C/LR-C) and quadrature phase-shifter (Q-PS). The two tunable couplers are in turn realized using a 2×2 MZI switch as shown in the inset of **Fig. 1**. Another tunable coupler (Back-Coupler, B-C) is also used at the end of the MZI to allow control over the residual imbalance in the optical field between the two arms of MZI caused by process variations. To monitor the ring resonance, 1% tap followed by an on-chip Ge-photodetector (PD) is used in each ring. Although this directly translates to increased passband loss of the filter, these taps are an integral part of the automatic software reconfiguration algorithm [7]. Another 10% monitor tap is used at the cross port of the filter for out-of-band-rejection tuning. The automatic calibration and tuning algorithm are implemented with the help of on-chip *thermo-optic phase-shifter or microheaters*. Both arm of the outer MZI, both rings and all the tunable couplers are loaded with a microheater.

As mentioned earlier, the three tunable couplers are realized using 2×2 MZI switches. The coupling matrix, C , for these switches is expressed as [18]

$$C = j e^{j\phi_A} \begin{bmatrix} \sin(\phi_D) & \cos(\phi_D) \\ \cos(\phi_D) & -\sin(\phi_D) \end{bmatrix} \triangleq j e^{j(\cos^{-1}(k)+\phi_{A_0})} \begin{bmatrix} \sqrt{t} & \sqrt{k} \\ \sqrt{k} & -\sqrt{t} \end{bmatrix} \quad (1)$$

Here, $\phi_A = \frac{\phi_U + \phi_L}{2} + \phi_{A_0}$ is the common-mode phase shift, $2\phi_D = \phi_U - \phi_L$ is the differential phase shift, and k and t are the cross and through optical power coupling coefficients respectively. The additional phase $\phi_{A_0} = \frac{2\pi c \Delta\tau}{n_{\text{eff}} \lambda}$ is due to the propagation delay, $\Delta\tau$, in the switch due to its

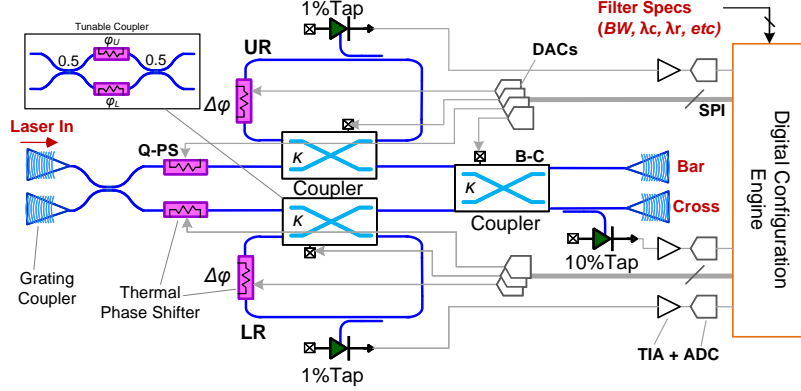


Fig. 1. Schematic of the silicon photonic filter and control electronics. The outer MZI is loaded with two rings coupled using a tunable coupler and includes microheater phase shifters. Another coupler is used to combine the two arms to compensate for any mismatches. Detector taps are placed at the drop port of the rings and on the filter cross port to assist the automatic reconfiguration algorithm. The inset shows the 2×2 switch used for realizing tunable couplers. Control electronics (DACs, TIAs and ADCs) are interfaced with digital configuration engine via SPI bus.

physical length. Here, n_{eff} is the effective index. Moreover, ϕ_U and ϕ_L , are the phase shifts induced in the upper and lower arm microheaters in the switch respectively. By tuning ϕ_D , we obtain the cross-coupling coefficient

$$k = \cos^2(\phi_D) = \frac{1}{2}[1 + \cos(2\phi_D)] \quad (2)$$

$$\triangleq \frac{1}{2}[1 + \cos(\varphi_0 + \gamma P_c)] \quad (3)$$

and the through-coupling coefficient $t = \sin^2(2\phi_D)$. The (cross)-coupling coefficient k is tuned by applying microheater electrical power, P_c , to one of the two microheaters in the switch (i.e. $\phi_U = 2\phi_D$ and $\phi_L = 0$). This implies the common-mode phase shift $\phi_A = \frac{\phi_U}{2} + \phi_{A_0} = \cos^{-1}(k) + \phi_{A_0}$. Also, here φ_0 represents the random phase offset in the switch and γ is a proportionality constant relating the applied power to the thermo-optic phase-shifter.

The z-domain through (all-pass) and drop (bandpass) transfer functions of a single ring in the filter seen in **Fig. 1** are derived as-

$$H_{\text{thru}}(z) = e^{j\phi_A} \cdot \frac{j\sqrt{t} - \sqrt{t_m}ae^{j(\phi+\phi_A)}z^{-1}}{1 + j\sqrt{t_m}ae^{j(\phi+\phi_A)}z^{-1}} \quad (4)$$

$$H_{\text{drop}}(z) = \frac{\sqrt{kk_m}e^{j\phi_A}z^{-1/2}}{1 + j\sqrt{t_m}ae^{j(\phi+\phi_A)}z^{-1}} \quad (5)$$

where $k_m = 0.01$ and $t_m = 0.99$ are the cross- and through-coupling coefficients for the 1% monitor, and $a = e^{-\alpha L} < 1$ is the loss factor in the ring. Waveguide loss α is 2.5 - 3dB/cm for the single-mode Si waveguide and L is the ring length. The 2^{nd} -order filter is realized using the coupled all-pass decomposition (APD) method and uses the phase difference between the upper and lower paths of the MZI to realize the desired polynomial magnitude response [16, 17]. The resulting filter output bar and cross transfer functions are

$$H_{APD2}(z) = \frac{j}{\sqrt{2}} \left(k_{bc} e^{j\phi_{q,ps}} H_{thru}(z) \Big|_{k_1, \phi_1} \pm t_{bc} e^{-j\phi_{q,ps}} H_{thru}(z) \Big|_{k_2, \phi_2} \right) \quad (6)$$

Here, k_n and ϕ_n are the power coupling coefficient and phase shift in the n^{th} ring, k_{bc} and $t_{bc} = 1 - k_{bc}$ are the back-coupler cross and through coupling coefficients, and $\phi_{q,ps}$ is the quadrature phase shift.

2.2. Fabrication, Packaging and Electronic Back-end

The filter was fabricated in a 300mm wafer AIM Photonics foundry's active photonics process [19]. This was part of AIM's active photonic MPW run (June, 2019). The process features SOI rib and ridge waveguides, and two layers of nitride waveguides, escalators, three levels of n and p doping, Germanium (Ge) detectors, and three metal layers for routing [19]. The filter schematic seen in **Fig. 1** was described in the previous section. The schematic was translated into PIC layout using process-optimized grating couplers, doped silicon thermo-optic phase shifters (microheaters), 50%, 10% & 1% couplers, Ge detectors and 2×2 switches from the PDK library. Single-mode silicon waveguides of 480nm width and 220nm height were used for routing and interconnecting the optical components. The total physical length of the rings are $\sim 2200\mu m$ each, resulting in an FSR of ~ 31 GHz.

The filter layout was compacted as much as possible to share the entire photonic chip with other photonic circuits. The filter core layout occupied an area of 1.12 mm^2 on the chip. The entire PIC die was thinned down to $150\mu m$ for better thermal management and packaged in a chip-on-board (COB) assembly (as shown in **Fig. 2**) along with the transimpedance amplifiers (TIAs), and ribbon-cable interfaces with commercial off the shelf (COTS) digital-to-analog converters (DACs) and analog-to-digital converters (ADCs). The electrical pads were placed on two rows on the East edge of the PIC. These pads provide DAC interfaces to the microheaters and monitor outputs to external TIAs.

A Peltier cell and thermistor were used along with a thermo-electric cooler (TEC) controller in a closed-loop to stabilize the temperature of the chip and to minimize the thermal crosstalk among the on-chip tuning elements. The combination of die thinning to $150\mu m$ and TEC at the bottom of the die provides effective thermal isolation by creating more prominent thermal gradient in the vertical direction [7]. The output of the on-chip monitors, i.e. Ge detectors, were fed to variable-gain TIAs followed by 16-bit ADCs, whereas the on-chip micro-heaters were driven by 16-bit DACs. All the DACs and ADCs communicate via SPI interface with a microcontroller which provides an interface between the DACs & ADCs and the algorithm code.

The operating voltage range of the microheaters is around 0 to 5V. These voltage ranges are **CMOS-compatible** and the microheater driver circuits can be implemented using stacked high-voltage I/O transistors with a 5V supply voltage in 65nm CMOS (or similar) process technology [20, 21]. The TIA interface with the PDs and the 16-bit DACs and ADCs can be designed using the standard transistors in CMOS, allowing future integration of all electronics on the same chip.

3. In-Situ Component Parameter Extraction

To reconfigure the SiP filter, device parameters such as the coupling ratio of the tunable couplers (k_n) and the ring phase bias (ϕ_n) for the selected center wavelength (λ_c) need to be configured. Here, $n = 1, 2, \dots, N$ stands for the ring number. These parameters are controlled by the DAC voltage (or power). Due to PVT variations in the photonic chip, there is a significant variation in the response of the tunable couplers and the phase shifters with respect to the applied power. Thus, no two couplers (or phase shifters) produce the same coupling (phase shift) for a given applied DAC voltage.

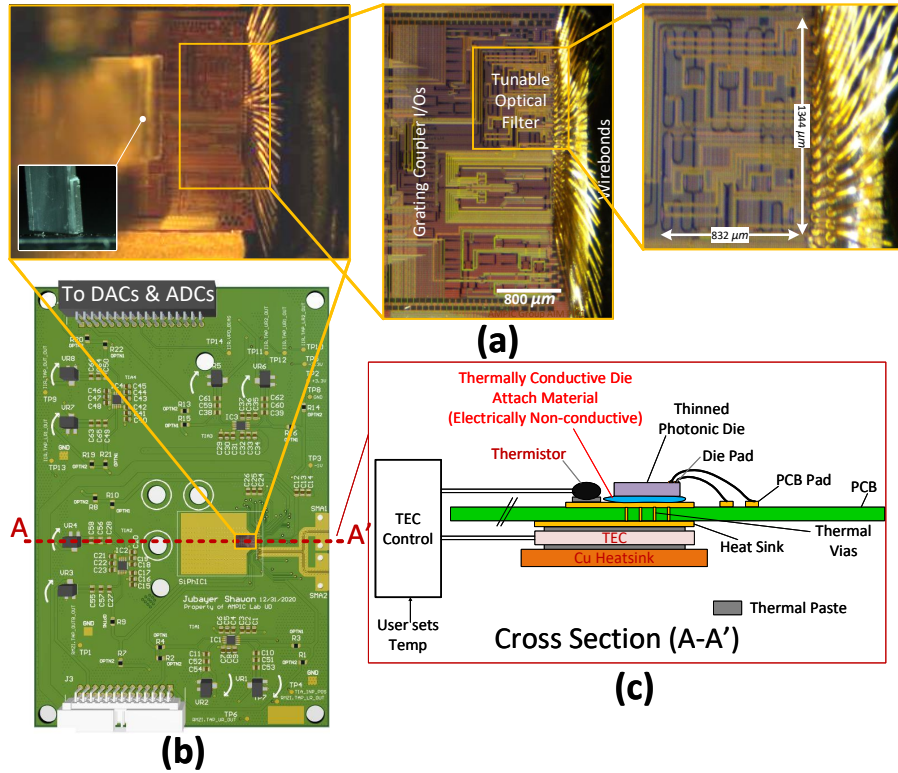


Fig. 2. (a) Chip micrograph of the silicon photonic filter fabricated in the AIM Photonics process. (b) The chip is attached and wirebonded onto a custom designed printed circuit board (PCB) using Chip-On-Board (COB) packaging. The PCB contains transimpedance amplifiers (TIAs) and ribbon cable interface to another electronic board with DACs and ADCs. (c) The COB assembly is co-packaged with a thermistor on the top-side and a Peltier cell on the back side of the PCB with an external TEC controller board in a closed loop.

The phase shift produced by the microheaters linearly depends upon the applied electrical power, P_n , *i.e.* $\phi_n = \gamma P_n$. However, the microheater resistance, R , exhibits nonlinearity due to self-heating. Thus, applied electrical power has a nontrivial nonlinear dependence on the applied DAC voltage, $P_n = f(v_n) \neq \frac{v_n^2}{R}$. This P_n vs v_n characteristics must also be extracted so that we can accurately configure component parameters on the chip using the DACs. This necessitates a one-time in-situ pre-characterization of each of these components, and subsequently the configuration of them, as they are used. In this section, we provide algorithms for these pre-characterization routines and configuration.

Each of these component characterization have two steps- Part I and II. The first part, Part I, for either k_n or ϕ_n extraction represents the component pre-characterization phase. On the other hand, during the automatic reconfiguration phase, this pre-characterized data is used for in-situ estimation and configuration of k_n and ϕ_n parameters in the on-chip filter. Part II algorithms for both k_n and ϕ_n represent these in-situ estimation and configuration.

It is important to note that Part I is a one-time operation and does not need to be repeated again as long as the filter ambient temperature is kept the same as the filter pre-characterization temperature. This is ensured by using the TEC setup seen in **Fig. 2**. On the other hand, Part II algorithms are invoked each time the filter is reconfigured or tuned to a different center frequency

(wavelength).

3.1. Coupling Ratio (k_n) Extraction

During the initial pre-characterization routine, **Algorithm 1** is executed for each of the n rings in the filter. Here, to be able to configure the desired coupling ratio (k_n) of the tunable coupler of the n^{th} ring, the wavelength response of the ring drop-port is recorded (using the monitor PDs) for a range of coupler input voltages ($v_{n,c}$). From this data, the voltage ($v_{n,cm}$) corresponding to the **maximum coupling ratio** ($k_{n,max}$) is recorded. The maximum coupling is identified by observing the quality factor (Q) of the ring drop-port resonance. Optical cavity dynamics dictate that as coupling ratio approaches unity, ring Q decreases [22]. This provides the basis for identifying the $k_{n,max}$ by observing the **minimum Q** (as shown in the bottom-right inset of **Fig. 3**). On the other hand, zero-coupling voltage ($v_{n,c0}$) is identified simply by finding the $v_{n,c}$ corresponding to lowest monitor output at a fixed $\lambda \in \Lambda$ (any wavelength within one FSR in the wavelength range of interest, *i.e.* Λ). This is possible due to the very low optical power coming through the drop-port when zero-coupling is in place (as shown in the top-left inset of **Fig. 3**). Afterwards, the power ($P_{n,c}$) delivered to n^{th} coupler microheater at different $v_{n,c}$ is recorded using a Keysight B2902A source measurement unit (SMU), and thus the $P_{n,c}$ vs $v_{n,c}$ characteristics are obtained.

Utilizing this data rather than simply relying on the quadratic relationship between voltage and power [23] ensures that the algorithm is insensitive to the electrical non-linearity of on-chip microheaters. Subsequently, the zero-coupling power ($P_{n,c0}$) and max-coupling heater power ($P_{n,cm}$) are obtained, and thus the power ($P_{n,c\pi}$) required to obtain a π phase shift in the coupler microheaters is determined as $P_{n,c\pi} = P_{n,cm} - P_{n,c0}$. This $P_{n,c\pi}$ will subsequently serve as a reference value for the tuning algorithm to operate at different wavelengths within the FSR of the rings. It is important to note that by utilizing zero and maximum coupling rather than the critical coupling as in [7], we avoid repeated re-centering of the ring resonance at the filter center frequency (λ_c) during the k_n extraction step. Also as mentioned earlier, use of an OVNA is avoided by precluding the ring loss measurements at critical coupling for each of the rings as in the prior art in [7]. This considerably speeds up the k_n extraction step in the filter reconfiguration algorithm ($\sim 2X$ reduction in time) and enables in-situ tuning that can be implemented using PCB-level or chip-scale electronics.

Algorithm 1 Coupling ratio extraction (Part I)

- 1: **Start**
 - 2: **Get** n^{th} Ring drop-port response, $f(\lambda, v_{n,c})$ & estimate Q
 - 3: $v_{n,cm}, P_{n,cm} \leftarrow$ **Find** $v_{n,c}, P_{n,c}$ corresponding to **min**(Q)
 - 4: **Set** laser wavelength at $\lambda \in \Lambda$
 - 5: **Get** n^{th} Ring drop-port response, $f(v_{n,c})$
 - 6: $v_{n,c0}, P_{n,c0} \leftarrow$ **Find** $v_{n,c}, P_{n,c}$ for zero coupling from **min**($f(v_{n,c})$)
 - 7: $P_{n,c\pi} \leftarrow P_{n,cm} - P_{n,c0}$
 - 8: **Save** $P_{n,c\pi}$
 - 9: **Save** $v_{n,c}$ vs $P_{n,c}$ characteristics
 - 10: **End**
-

During the in-situ reconfiguration routine in **Algorithm 2**, first the $P_{n,c0}$ is recorded, and depending on the λ_c , this may not be the same as the $P_{n,c0}$ seen in **Algorithm 1**. Then, the raised-cosine coupling ratio vs power curve of the tunable coupler [7] from **Eq. 3** and illustrated in **Fig. 3** is fitted to the $(P_{n,c0}, 0)$ & $(P_{n,c0} + P_{n,c\pi}, k_{n,max})$ data points. From this fitted curve, power ($P_{n,c}^*$) required to set any desired coupling ratio (k_n) is estimated as shown in **Fig. 3**. Afterwards, from the pre-characterization $v_{n,c}$ vs $P_{n,c}$ data, the DAC voltage ($v_{n,c}^*$) needed to

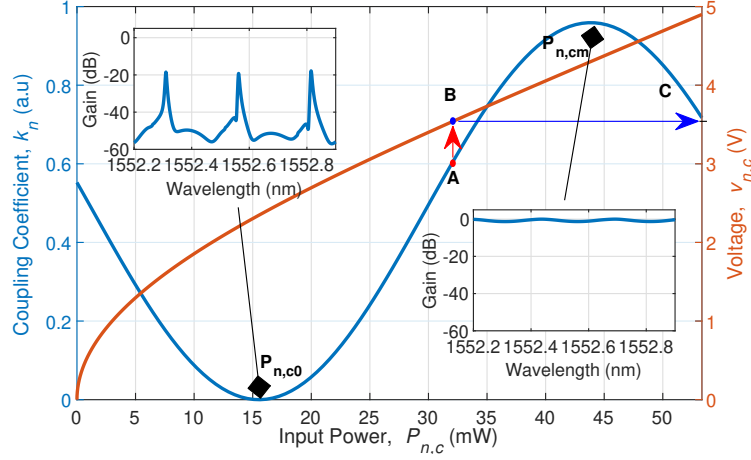


Fig. 3. (Illustration of Algorithms 1 and 2): Coupling coefficient, k_n , of a tunable coupler with a process induced random phase offset and the microheater voltage as a function of input power, $P_{n,c}$, as expressed by Eq. 3. The top-left and bottom-right insets show normalized wavelength response of the ring drop port with its coupler set at zero ($P_{n,c} = P_{n,c0}$ & $k = 0$) and maximum coupling ratio ($P_{n,c} = P_{n,cm}$ & $k = k_{n,max}$), respectively. Any desired value for $k = k_n$ (labeled as A) can be in-situ configured by applying the corresponding input power, $P_{n,c}^*$ (label B), which in turn is translated to the DAC voltage, $v_{n,c}^*$ (label C).

set a desired k_n is determined. Here, $k_{n,max}$ is the maximum coupling coefficient and due to the intrinsic loss in the coupler, it never reaches unity. For our tunable coupler, it is found to be 0.959 from the foundry PDK. Furthermore, for the purpose of the filter and its usable frequency range for a free-spectral range (FSR) of 31 GHz (or 0.249 nm), the couplers can be considered broadband. Thus, all the extracted parameters are usable at any frequency (or wavelength) within the FSR.

Algorithm 2 Coupling ratio extraction (Part II)

- 1: **Input:** $k_n \leftarrow$ User specifies the desired coupling coefficient
 - 2: **procedure** `ccoeff`(n, λ_c, k_n)
 - 3: **Set** laser wavelength at λ_c
 - 4: **Get** n^{th} Ring drop-port response, $f(v_{n,c})$
 - 5: $v_{n,c0}, P_{n,c0} \leftarrow$ **Find** $v_{n,c}, P_{n,c}$ for zero coupling from $\min(f(v_{n,c}))$
 - 6: **Fit** k_n vs $P_{n,c}$ in Eq. 3 using $(P_{n,c0}, 0)$ & $(P_{n,c0} + P_{n,c\pi}, k_{n,max})$ data points
 - 7: $P_{n,c}^* \leftarrow$ **Find** power for k_n from the above curve-fit
 - 8: $v_{n,c}^* \leftarrow$ **Find** voltage corresponding to $P_{n,c}^*$ from the $v_{n,c}$ vs $P_{n,c}$ data
 - 9: **Return** n^{th} coupler DC bias, $v_{n,c}^*$
 - 10: **End procedure**
-

3.2. Ring Phase (ϕ_n) Extraction

Now we describe the one-time pre-characterization routine (i.e. **Algorithm 3**) for the ring phase bias. First, all the rings except for the n^{th} ring are detached from the filter by setting their corresponding couplers to zero-coupling. This ensures that the cross-port of the filter only shows the resonance response of the n^{th} ring. Then, the voltage ($v_{n,r\pi}$) required for a π phase shift in the

ring microheater was extracted by monitoring the cross port of the filter and shifting the resonance by full FSR (corresponding to 2π phase-shift in the ring) for the applied voltage. Afterwards, the power ($P_{n,r}$) delivered to n^{th} ring heater at different $v_{n,r}$ is recorded using the SMU and $P_{n,r\pi}$ is obtained. As mentioned before, utilizing $v_{n,r}$ vs $P_{n,r}$ data ensures that the algorithm is insensitive to the process-dependent electrical nonlinearity of the on-chip microheaters.

Algorithm 3 Ring phase extraction (Part I)

- 1: **Start**
 - 2: **Set** $v_{i,c} \leftarrow$ **Find** $v_{i,c0}$ for all couplers except when $i = n$
 - 3: **Get** filter bar-port response, $f(\lambda, v_{n,r})$
 - 4: $v_{n,r\pi}, P_{n,r\pi} \leftarrow$ **Find** $v_{n,r}, P_{n,r}$ for π phase-shift, obtained using a full-FSR sweep
 - 5: **Save** $P_{n,r\pi}$
 - 6: **Save** $v_{n,r}$ vs $P_{n,r}$ data
 - 7: **End**
-

During the automatic calibration routine in **Algorithm 4**, pre-characterized $P_{n,r\pi}$, and $v_{n,r}$ vs $P_{n,r}$ characteristics of the ring microheater is utilized. Then, from the phase-shift desired by the user, ϕ_n , the required microheater power change ($\Delta P_{n,r} = \frac{\phi_n P_{n,r\pi}}{\pi}$) is estimated. Meanwhile, the voltage ($v_{n,res}$) for which the n^{th} ring resonance is aligned with λ_c is obtained by sweeping the ring microheater voltage ($v_{n,r}$) and finding the maximum drop port response. From this data, the power ($P_{n,res}$) at which ring resonance is aligned with λ_c is obtained. Then, the power ($P_{n,r}^*$) required to set the ring at desired ϕ_n is estimated as $P_{n,r}^* = P_{n,res} + \Delta P_{n,r}$ and the corresponding ring microheater voltage ($v_{n,r}^*$) is applied.

Algorithm 4 Ring phase extraction (Part II)

- 1: **Input:** $\phi_n \leftarrow$ User specifies the desired ring phase
 - 2: **procedure** **ringbias**(n, λ_c, ϕ_n)
 - 3: $\Delta P_{n,r} \leftarrow \frac{\phi_n P_{n,r\pi}}{\pi}$
 - 4: **Set** laser wavelength at λ_c
 - 5: **Get** n^{th} Ring drop-port response, $f(v_{n,r})$
 - 6: $v_{n,res}, P_{n,res} \leftarrow$ **Find** $v_{n,r}, P_{n,r}$ for **max**($f(v_{n,r})$) ▷ resonance
 - 7: $P_{n,r}^* \leftarrow P_{n,res} + \Delta P_{n,r}$
 - 8: $v_{n,r}^* \leftarrow$ **Find** voltage for $P_{n,r}^*$ from the $v_{n,r}$ vs $P_{n,r}$ data
 - 9: **Return** n^{th} ring heater DC bias $v_{n,res}$ & $v_{n,r}^*$
 - 10: **End procedure**
-

4. Automatic Tuning of Filters

The filter tuning algorithm (**Algorithm 5**) starts off with the user specifying the desired filter specifications. The APD filter synthesis algorithm [17, 24] translates these user-defined specifications (filter type, order, bandwidth, center frequency, out-of-band suppression) to filter parameters (k_n, ϕ_n & $\phi_{q,ps}$) for all rings and MZI arms. Then the **ccoeff**(n, λ_c, k_n) routine from **Algorithm 2** is invoked and desired coupling coefficients for all ring couplers are configured by setting the microheater voltages of the ring tunable couplers to $v_{n,c}^*$. Next, the **ringbias**(n, λ_c, ϕ_n) routine from **Algorithm 4** is invoked to set all the ring biases (ϕ_n) with respect to the λ_c at their desired values. It's important to note that due to thermal crosstalk between on-chip microheaters, every time a ring phase (ϕ_n) is set, previously aligned rings get de-tuned and several iterations are required accurately to set all the ϕ_n values.

To improve the out-of-band rejection of the filter, we maximize the 10% monitor tap placed at the cross-port of the filter at λ_r by tuning the MZI quadrature-phase-shifter (Q-PS) and the back-coupler (B-C). Here, λ_r is the wavelength where a null in the filter response can be enforced.

However, the out-of-band-rejection calibration via Q-PS and B-C microheaters shifts the resonance of the previously tuned rings, thus altering the center wavelength (or frequency) of the filter response. To perform center-wavelength correction, rings, Q-PS and B-C are tuned subsequently and several iterations of tuning (n rings, Q-PS and B-C) are needed to reach the thermal steady-state of the PIC. When the required voltage stimulus is stabilized within a tolerance range (indicating a thermal steady-state), the filter tuning is complete.

It's important to note that the coupling ratio of the tunable couplers are relatively stable in presence of thermal perturbation. This is due to the fact that thermal perturbation coming from other microheaters affect both microheaters of the tunable couplers almost equally, thus inducing a 'common-mode' phase shift that does not alter the coupling ratios which only depends upon the differential phase (ϕ_D). Therefore, it is not required to include ring coupler tuning inside the iteration loop, which in turn speeds up the reconfiguration process. Another key aspect of this algorithm is that it precludes the use of 'outer ring' for out-of-band rejection in [7], thus further reducing configuration time for 'outer ring' resonance alignment and also results in a smaller layout area.

5. Experimental Results

To demonstrate the functionality and efficacy of the proposed reconfiguration algorithm, we present a 2^{nd} -order Butterworth filter with ~ 30 dB rejection, insertion loss (IL) of 2.2 dB, and the 3dB bandwidth (BW) of 3 GHz around 1550nm wavelength. A laser output at C-band (1550nm) was coupled in and out of the PIC using fiber array that is automatically aligned to the on-chip grating couplers. The corresponding filter coefficients generated by the APD filter synthesis algorithm are presented in **Table 1**.

Table 1. Filter Coefficients generated by coupled all-pass decomposition (APD) filter synthesis for the filter schematics seen in Fig. 1.

Ring (n)	k_n	ϕ_n	$\phi_{q,ps}$
1 (UR)	0.4385	-0.2969	Top: -1.6137
2 (LR)	0.4385	0.2969	Bot: 1.6137

The experimentally measured response of the filter at different stages of reconfiguration is illustrated in **Fig. 4**. Here, the grating coupler passband losses are de-embedded from the filter response. Unlike [7], here in this work, as soon as the Q-PS and/or B-C microheater is tuned, the previously locked UR & LR rings get de-tuned due to thermal crosstalk and the center frequency of the filter shifts from its intended λ_c (in this case, $\lambda_c = 1550$ nm) as demonstrated in **Fig. 4**(d) and (e). Therefore, several iterations are required for automatic tuning of the filter.

Since DACs set the microheater voltages (or power), the convergence of the tuning algorithm can be observed in the settling of the DAC output voltages. In **Fig. 5**, the transient evolution of DAC voltages for all relevant microheaters during the tuning process is presented. **Fig. 5** also shows the laser wavelength settings (λ_c and λ_r) that are applied to the filter input. Key events that occur during the automatic tuning process are labeled in **Fig. 5** and explained in **Table 2**. This figure shows three iterations to tune the filter (rings, Q-PS & B-C), and the time taken for the iteration progressively decreases as the filter gets closer to the thermal steady-state during tuning. In our filter layout, the Q-PS and B-C coupler was in close proximity to the rings resulting in substantial thermal crosstalk. The fabricated 2^{nd} -order filter takes around 725 seconds to tune

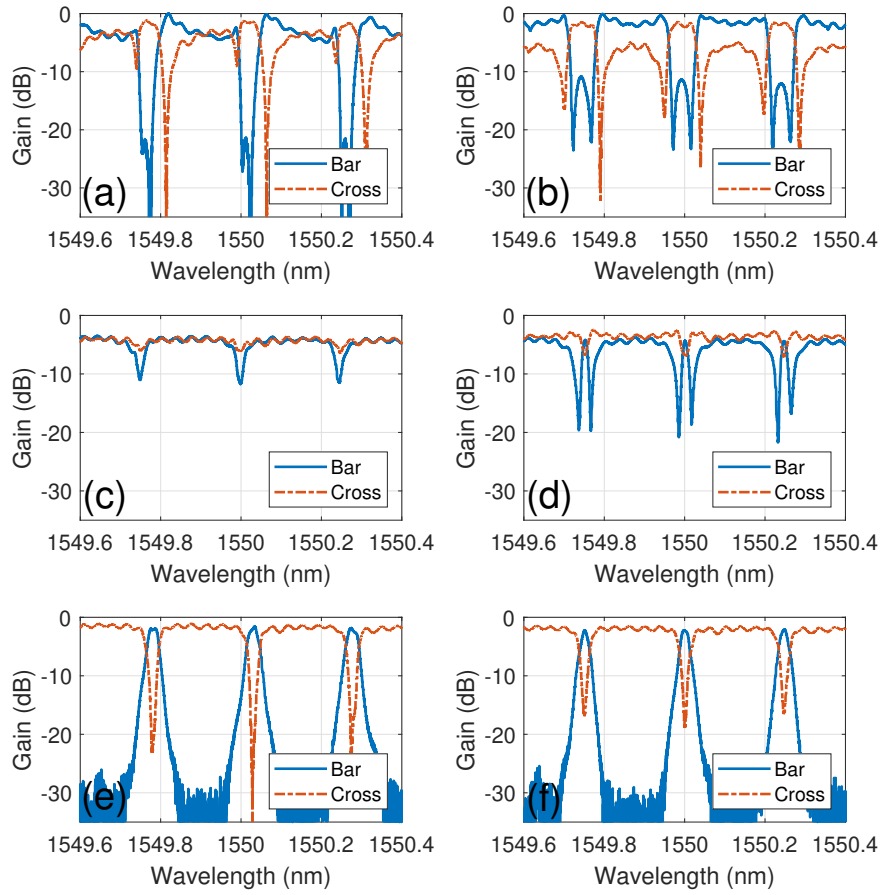


Fig. 4. Experimentally measured bar and cross port responses (normalized) of the filter: (a) When powered up without any tuning, (b) After all the coupling ratios (k_n) of the rings are configured (Algorithm 2), (c) After aligning the ring resonances to λ_c (part of Algorithm 4), (d) After setting desired phase bias (ϕ_n) of the rings (part of Algorithm 4), (e) After Quadrature Phase-Shifter (Q-PS) and Back-Coupler (B-C) tuning, (f) After center frequency correction i.e. several iterations of ring phase bias (ϕ_n), Q-PS and B-C tuning.

Algorithm 5 N^{th} Order Filter reconfiguration Algorithm

```
1: Start
2: Get Filter specifications (Type, Order, BW, Rejection,  $\lambda_c$ ,  $\lambda_r$ ) from the user
3:  $k_n, \phi_n, \phi_{q,ps} \leftarrow$  APD filter synthesis using the specifications
4: Set  $n = 1$ 
5: while  $n \leq N$  do
6:   Invoke  $[v_{n,c}^*] = \text{ccoeff}(n, \lambda_c, k_n)$  routine
7:   Set  $v_{n,c}^* \leftarrow$  DC bias of  $n^{th}$  coupler
8:   Set  $n = n + 1$ 
9: end while
10: Set  $n = 1$ 
11: while  $\text{err}_j \geq \text{tol}_j$  do
12:   while  $\text{err}_i \geq \text{tol}_i$  do
13:     while  $n \leq N$  do
14:       Invoke  $[v_{n,res}, v_{n,r}^*] = \text{ringbias}(n, \lambda_c, \phi_n)$ 
15:       Set  $v_{n,res} \leftarrow$  DC bias for  $n^{th}$  ring resonance
16:       Set  $n = n + 1$ 
17:     end while
18:     Calculate  $\text{err}_i$ 
19:   end while
20:   Set  $v_{n,r}^* \leftarrow$  DC bias of  $n^{th}$  ring
21:   Set Laser wavelength at  $\lambda_r$ 
22:   Get filter cross-port PD response,  $f(v_{q,ps})$ 
23:    $v_{q,psm} \leftarrow$  Find  $v_{q,ps}$  for max  $f(v_{q,ps})$ 
24:   Set DC bias of the arm phase shifter at  $v_{q,psm}$ 
25:   Get filter cross-port PD response,  $f(v_{b,c})$ 
26:    $v_{b,cm} \leftarrow$  Find  $v_{b,c}$  for max  $f(v_{b,c})$ 
27:   Set DC bias of back-end tunable coupler at  $v_{b,cm}$ 
28:   Calculate  $\text{err}_j$ 
29: end while
30: End
```

for the first time. The long configuration times are primarily determined by the thermal crosstalk between the components and can be significantly reduced by spreading out the layout and by employing microheaters with undercut for better thermal isolation [25,26].

As mentioned earlier, for software defined radios (SDR) and flexible RF photonic receivers, it is vital to have filters with agile center-frequency and bandwidth tunability. To demonstrate such capability, we reconfigured the filter at 5 different center frequencies (λ_c) with 0.05nm (~ 6.25 GHz) spacing as shown in **Fig. 6** (top). It's important to note that the center frequency tuning is continuous and any center wavelength (λ_c) can be configured as long as it is within the FSR of the rings. This means that the fabricated filter can be reconfigured at any frequency between DC and 31 GHz. To cover higher frequency bands, the filter can be redesigned with smaller rings (i.e. larger FSR). On the other hand, the bandwidth (BW) tunability of our proposed filter is shown in **Fig. 6** (bottom) for BW = 2.68, 3 and 3.69 GHz. A trade-off can be observed in **Fig. 6** (bottom), whereby as the BW is reduced, the passband insertion loss increases [13]. This becomes even more prominent when sub-GHz 3dB bandwidth settings are attempted. This is due to the losses in the rings, and can be mitigated by adopting low-loss multimode waveguide design [27] and/or utilizing the upcoming ultra low-loss PDK from AIM Photonics [19].

In **Table 3**, a comparison of this work with other related work such as 2^{nd} -order APD filter [7],

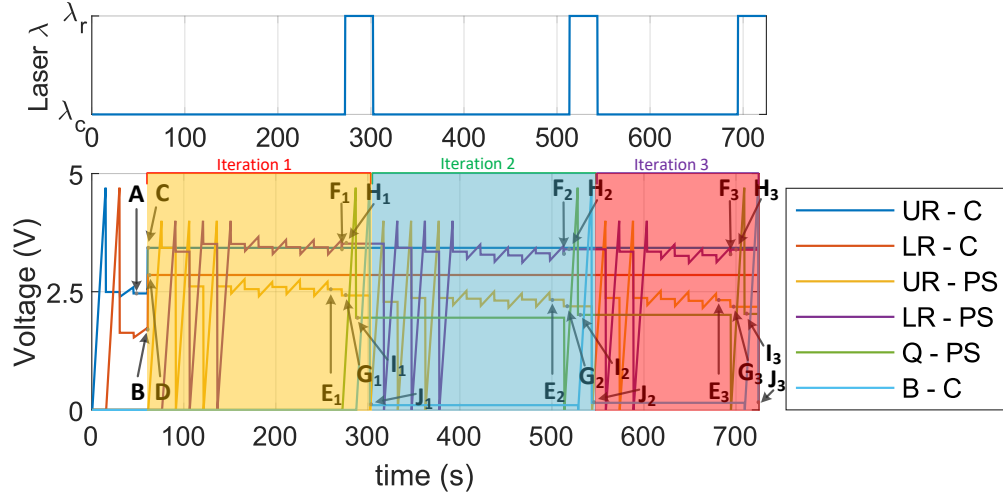


Fig. 5. DAC sampling and laser wavelength switching at different stages of silicon photonic filter reconfiguration. The corresponding timestamps are explained in detail in Table 2. Each iteration corresponds to ring phase, quadrature phase-shifter and back-coupler configuration steps. Here, three iterations were needed as the thermal crosstalk from the last back-coupler and quadrature phase-shifter configuration step de-tunes the rings.

Table 2. Explanation of DAC tuning events.

Event	Details
A	Upper Ring coupler (UR-C) is set to zero coupling after a coarse and fine search.
B	Lower Ring coupler (LR-C) is set to zero coupling after a coarse and fine search.
C	Upper Ring coupler (UR-C) is set to desired coupling ratio based on Algorithm 2 .
D	Lower Ring coupler (LR-C) is set to desired coupling ratio based on Algorithm 2 .
E_n	n^{th} iteration of Upper Ring phase-shifter (UR-PS) resonance alignment to λ_c after coarse and fine search.
F_n	n^{th} iteration of Lower Ring phase-shifter (LR-PS) resonance alignment to λ_c after coarse and fine search.
G_n	n^{th} iteration of configuring Upper Ring phase-shifter (UR-PS) phase bias ϕ_1 based on Algorithm 4 .
H_n	n^{th} iteration of configuring Lower Ring phase-shifter (LR-PS) phase bias ϕ_2 based on Algorithm 4 .
I_n	n^{th} iteration of maximizing 10% monitor tap output by tuning Quadrature phase-shifter (Q-PS).
J_n	n^{th} iteration of maximizing 10% monitor tap output by tuning Back-coupler (B-C).

4th-order APD filter [7], 5th-order CROW filter [10], 2nd-order CROW filter [11], 4th-order APD filter [13] has been presented. As evident from the comparison, this work presents a first fully-automatic filter tuning scheme with in-situ reconfiguration capability.

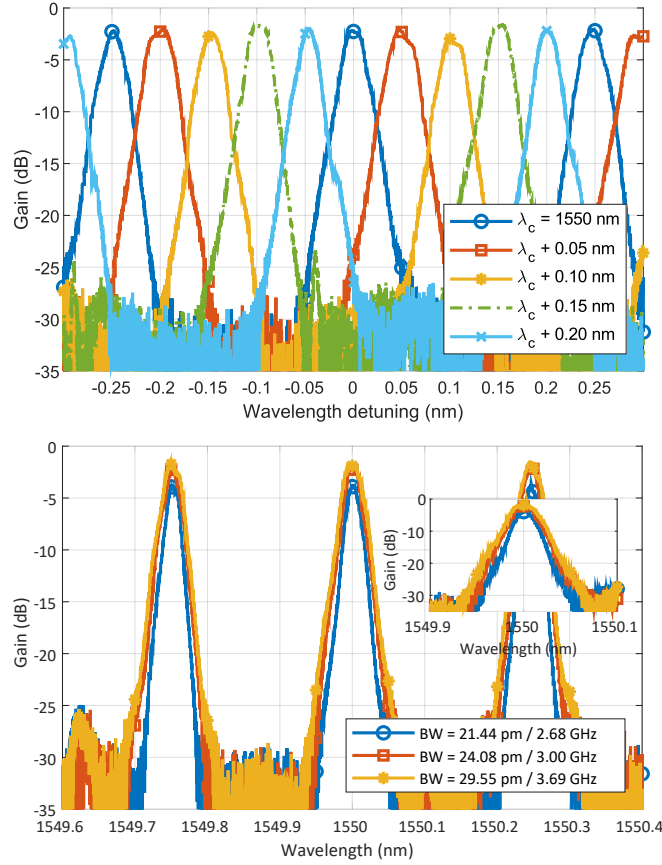


Fig. 6. (Top) Center frequency tuning of the silicon photonic filter. Here, the filter is configured at 5 different wavelengths with $\Delta\lambda = 0.05$ nm or $\Delta f = 6.25$ GHz. (bottom) Bandwidth Tuning of the filter around $\lambda_c = 1550$ nm.

6. Conclusion and Future Work

This work presented a robust silicon photonic filter for RF photonic applications with an improved reconfiguration algorithm that is insensitive to PVT variations. By utilizing proposed in-situ configuration algorithm with simpler pre-characterization steps (no need for OVNA), we have experimentally shown that the filter can be configured to any desired center frequency, bandwidth and rejection as per the user specifications with high fidelity. Moreover, the filter is a first of its class to be fabricated in AIM photonics's CMOS compatible Active Photonic process, making the filter widely manufacturable at low cost for next-generation RF photonic systems. The proposed coupling coefficient extraction and configuration algorithm provides upto 2X improvement in configuration time over the prior art.

Further improvements such as sub-GHz bandwidth with low insertion loss can potentially be achieved by incorporating multimode & low-loss waveguide designs [27] and <1% monitor taps in the rings, and/or leveraging the planned ultra-low-loss PDK and MPW runs from AIM Photonics [19]. The current 2nd-order filter initial reconfiguration time is around 725s. With

Table 3. Comparison with state-of-the art in filter tuning.

Metric	This Work.	Ref. [7]	Ref. [7]	Ref. [10]	Ref. [11]	Ref. [13]	
Technology	AIM	IME SiP	IME SiP	IME SiP	IME SiP	BAE SiP	
Architecture	APD	APD	APD	CROW	CROW	APD	
Order	2	2	4	5	2	4	
FSR (nm)	0.249 (31 GHz)	0.396 (50 GHz)	0.396 (50 GHz)	~2.47 (308 GHz)	2.10 (265 GHz)	0.1307 (16.5 GHz)	
BW (GHz)	3	6.89	5	~30.9	33.4	1	
Rejection (dB)	30	32	33	~50	25	25	
Passband Insertion Loss (dB)	2.2	~2.3	4.67	~2.64	2.11	6	
Reconfigurability	f_c	Y	Y	Y	Y	Y	Y
	BW	Y	Y	Y	N	Y	Y
	Rejection	Y	Y	Y	N	N	Y
Automatic Reconfiguration	f_c	Y	Y	Y	Y	Y	N
	BW	Y	Y	Y	N	Y	N
	Rejection	Y	Y	Y	N	N	N
Portability	No OVNA	Uses OVNA	Uses OVNA	-	-	-	

our optimized algorithm and a low thermal crosstalk design where back-coupler and quadrature phase shifter tuning does not affect the ring bias (ϕ_n) as in [7], the filter reconfiguration time can be as fast as ~ 300 s. This can be achieved by careful planning of PIC layout where the thermo-optic phase-shifters (microheaters) are placed further apart from sensitive waveguides (rings) at the expense of a larger footprint. Achieving rapid filter reconfiguration on the order of seconds in frequency-agile SDRs will require even higher thermal isolation between on-chip photonic components. This can potentially be achieved by integration of microheaters with undercut [26] in the SiP foundry process. In summary, by taking full advantage of the large-volume low-cost manufacturing of a CMOS-compatible photonic process, the presented RF photonic filters and improved reconfiguration algorithm provide a way forward for wider adoption in high-performance RF and microwave photonic transceivers.

Funding. This work was supported by the Air Force Office of Sponsored Research (AFOSR) YIP Award FA9550-17-1-0076, DARPA YFA Award HR00112110001 and National Science Foundation (NSF) CAREER Award EECS-2014109.

Disclosures. The authors declare no conflicts of interest.

Data Availability Statement. Data underlying the results presented in this paper are not publicly available at this time but may be obtained from the authors upon reasonable request.

References

1. J. Capmany, G. Li, C. Lim, and J. Yao, "Microwave photonics: current challenges towards widespread application," *Opt. express* **21**, 22862–22867 (2013).
2. V. J. Urick, K. J. Williams, and J. D. McKinney, *Fundamentals of microwave photonics* (John Wiley & Sons, 2015).
3. X. Yi, S. X. Chew, S. Song, L. Nguyen, and R. Minasian, "Integrated microwave photonics for wideband signal processing," in *Photonics*, vol. 4 (Multidisciplinary Digital Publishing Institute, 2017), p. 46.
4. R. A. Minasian, E. Chan, and X. Yi, "Microwave photonic signal processing," *Opt. Express* **21**, 22918–22936 (2013).

5. D. Marpaung, C. Roeloffzen, R. Heideman, A. Leinse, S. Sales, and J. Capmany, "Integrated microwave photonics," *Laser & Photonics Rev.* **7**, 506–538 (2013).
6. W. Zhang and J. Yao, "Silicon-based integrated microwave photonics," *IEEE J. Quantum Electron.* **52**, 1–12 (2015).
7. G. Choo, S. Cai, B. Wang, C. K. Madsen, K. Entesari, and S. Palermo, "Automatic monitor-based tuning of reconfigurable silicon photonic apf-based pole/zero filters," *J. Light. Technol.* **36**, 1899–1911 (2018).
8. R. Won, "Integrating silicon photonics," *Nat. photonics* **4**, 498–499 (2010).
9. W. Bogaerts and L. Chrostowski, "Silicon photonics circuit design: methods, tools and challenges," *Laser & Photonics Rev.* **12**, 1700237 (2018).
10. J. C. Mak, W. D. Sacher, T. Xue, J. C. Mikkelsen, Z. Yong, and J. K. Poon, "Automatic resonance alignment of high-order microring filters," *IEEE J. Quantum Electron.* **51**, 1–11 (2015).
11. J. C. Mak, A. Bois, and J. K. Poon, "Programmable multiring butterworth filters with automated resonance and coupling tuning," *IEEE J. Sel. Top. Quantum Electron.* **22**, 232–240 (2016).
12. B. Guan, S. S. Djordjevic, N. K. Fontaine, L. Zhou, S. Ibrahim, R. P. Scott, D. J. Geisler, Z. Ding, and S. B. Yoo, "Cmos compatible reconfigurable silicon photonic lattice filters using cascaded unit cells for rf-photonics processing," *IEEE J. Sel. Top. Quantum Electron.* **20**, 359–368 (2013).
13. M. S. Rasras, D. M. Gill, S. S. Patel, K.-Y. Tu, Y.-K. Chen, A. E. White, A. T. Pomerene, D. N. Carothers, M. J. Grove, D. K. Sparacin, J. Michel, M. A. Beals, and L. C. Kimerling, "Demonstration of a fourth-order pole-zero optical filter integrated using CMOS processes," *J. Light. Technol.* **25**, 87–92 (2007).
14. S. Liao, Y. Ding, C. Peucheret, T. Yang, J. Dong, and X. Zhang, "Integrated programmable photonic filter on the silicon-on-insulator platform," *Opt. Express* **22**, 31993–31998 (2014).
15. J. Kim, W. J. Sung, O. Eknoyan, and C. K. Madsen, "Linear photonic frequency discriminator on a 2 s 3-ring-on-ti Linbo 3 hybrid platform," *Opt. Express* **21**, 24566–24573 (2013).
16. P. A. Regalia, S. K. Mitra, and P. Vaidyanathan, "The digital all-pass filter: A versatile signal processing building block," *Proc. IEEE* **76**, 19–37 (1988).
17. C. Madsen, "Efficient architectures for exactly realizing optical filters with optimum bandpass designs," *Photonics Technol. Lett. IEEE* **10**, 1136–1138 (1998).
18. J. Capmany and D. Pérez, *Programmable Integrated Photonics* (Oxford University Press, 2020).
19. "Aim photonics, url: <http://www.aimphotonics.com/pdk/>,"
20. C. Li, K. Yu, J. Rhim, K. Zhu, N. Qi, M. Fiorentino, T. Pinguet, M. Peterson, V. Saxena, and S. Palermo, "A 3d-integrated 56 gb/s nrz/pam4 reconfigurable segmented mach-zehnder modulator-based si-photonics transmitter," in *2018 IEEE BiCMOS and Compound Semiconductor Integrated Circuits and Technology Symposium (BCICTS)*, (IEEE, 2018), pp. 32–35.
21. K. Zhu, V. Saxena, X. Wu, and W. Kuang, "Design considerations for traveling-wave modulator-based cmos photonic transmitters," *IEEE Transactions on Circuits Syst. II: Express Briefs* **62**, 412–416 (2015).
22. W. Bogaerts, P. De Heyn, T. Van Vaerenbergh, K. De Vos, S. Kumar Selvaraja, T. Claes, P. Dumon, P. Bienstman, D. Van Thourhout, and R. Baets, "Silicon microring resonators," *Laser & Photonics Rev.* **6**, 47–73 (2012).
23. H. Li, G. Balamurugan, M. Sakib, R. Kumar, H. Jayatileka, H. Rong, J. Jaussi, and B. Casper, "12.1 a 3d-integrated microring-based 112gb/s pam-4 silicon-photonics transmitter with integrated nonlinear equalization and thermal control," in *2020 IEEE International Solid-State Circuits Conference-ISSCC*, (IEEE, 2020), pp. 208–210.
24. M. J. Shawon and V. Saxena, "Rapid simulation of photonic integrated circuits using verilog-a compact models," in *2019 IEEE 62nd International Midwest Symposium on Circuits and Systems (MWSCAS)*, (IEEE, 2019), pp. 424–427.
25. A. Masood, M. Pantouvaki, G. Lepage, P. Verheyen, J. Van Campenhout, P. Absil, D. Van Thourhout, and W. Bogaerts, "Comparison of heater architecture for thermal control of silicon photonics circuits," in *IEEE Group IV Photonics*, (2013), pp. 83–84.
26. D. Coenen, H. Oprins, Y. Ban, F. Ferraro, M. Pantouvaki, J. Van Campenhout, and I. De Wolf, "Thermal modelling of silicon photonic ring modulator with substrate undercut," *J. Light. Technol.* (2022).
27. D. Onural, H. Gevorgyan, B. Zhang, A. Khilo, and M. A. Popović, "Ultra-high q resonators and sub-ghz bandwidth second order filters in an soi foundry platform," in *Optical Fiber Communication Conference*, (Optical Society of America, 2020), pp. W1A–4.